Atmos. Chem. Phys., 26, 1–13, 2026
https://doi.org/10.5194/acp-26-1-2026


Atmospheric Chemistry and Physics
Open Access
EGU



# Morphology-dependent stratocumulus susceptibilities revealed by a continuous morphology framework

**Tom Goren**[1], **Goutam Choudhury**[1], **and Graham Feingold**[2]

[1]Department of Environment, Planning and Sustainability, Bar-Ilan University, Ramat Gan, Israel
[2]NOAA, Chemical Sciences Laboratory, Boulder, CO, USA

**Correspondence:** Tom Goren (tom.goren@biu.ac.il)

Received: 7 January 2026 – Discussion started: 8 January 2026
Revised: 17 April 2026 – Accepted: 21 April 2026 – Published:

**Abstract.** We introduce a new framework for defining marine stratocumulus cloud morphologies using a ternary diagram. A ternary diagram is a triangular representation of three components, with each vertex corresponding to 100 % of one component, and any point within the triangle representing a mixture of all three that sums to 100 %. We use cloud optical thickness ($\tau_c$) as the diagnostic physical variable and accordingly define three corresponding $\tau_c$ classes. Different combinations of the three $\tau_c$ classes define different cloud morphologies, which vary continuously within the ternary space. The method is applied to one year of satellite observations of stratocumulus clouds and reveals the frequency of occurrence of the different morphologies across the ternary space. Large-eddy simulations complement the satellite analysis and show that cloud evolution tends to follow preferred paths across the ternary morphology space, explaining why the observations are concentrated within a limited range of morphologies. We further investigate the susceptibility of cloud liquid water path (LWP), cloud albedo, and cloud fraction to variations in droplet number concentration, conditioned on cloud morphology. We find that susceptibilities vary strongly with cloud morphology, yet in the most frequently occurring scenes, LWP and cloud albedo susceptibilities largely offset each other, resulting in a near-zero global in-cloud albedo response. We also find that cloud fraction susceptibility can be negative in low-LWP morphologies, presumably due to strong negative LWP adjustments. These findings have important implications for marine cloud brightening, whose effectiveness needs to be evaluated in a morphology-dependent framework to achieve the intended outcomes.

## 1 Introduction

Cloud albedo ($A_c$) is mainly determined by the liquid water path (LWP) and cloud droplet size. To first order these two properties set the cloud optical thickness ($\tau_c$), which is the primary quantity controlling $A_c$. Aerosols can influence both LWP and droplet size, and thus $A_c$: An increase in aerosol concentration can raise the cloud droplet concentration ($N_d$), which reduces droplet size, given no change in cloud water (Twomey, 1974). This leads to an increase in $A_c$ through a well-established physical mechanism (Platnick and Twomey, 1994; Twomey, 1974). This sensitivity of $A_c$ to $N_d$ is termed the cloud albedo susceptibility, $S_{A_c}$. An increase in $N_d$ can also initiate processes that influence the cloud water, which in turn also changes $A_c$ (Ackerman et al., 2004; Albrecht, 1989; Bretherton et al., 2007). This latter effect, the LWP susceptibility to $N_d$, $S_{LWP}$, is termed LWP adjustment. Its sign and magnitude remain uncertain due to the complexity of the underlying processes (Glassmeier et al., 2021; Bellouin et al., 2020; Forster et al., 2021; Toll et al., 2019; Goren et al., 2025). Positive LWP adjustments amplify the cloud albedo response to $N_d$, whereas negative LWP adjustments counteract it. The combined effects of the cloud albedo response and LWP adjustments to changes in $N_d$ determine the net in-cloud albedo susceptibility, $S_{net}$, which is the quantity that matters for the radiation budget of the Earth.

Cloud albedo varies spatially from meter scales up to hundreds of kilometers (Davis et al., 1997; Rampal and Davies, 2020; Stevens et al., 2020; Wood, 2006; Zhou et al., 2021). These spatial variations manifest as different cloud mor-

phologies (Goren et al., 2023; McCoy et al., 2017; Eastman et al., 2024; Wood and Hartmann, 2006; Choudhury and Goren, 2024). Studies that classify stratocumulus cloud morphologies typically define discrete morphology regimes such as open cells, closed cells, and disorganized mesoscale cellular convection (Wood and Hartmann, 2006; Muhlbauer et al., 2014; Erfani and Hosseinpour, 2025; Wu et al., 2025; Yuan et al., 2020; Geiss et al., 2024). Nevertheless, there is a continuum of morphologies between these discrete regime definitions (McCoy et al., 2023; Choudhury and Goren, 2024; Goren et al., 2023), and even fully overcast closed cells, which are typically classified as a single morphology regime, can exhibit structural differences, for example with cells having different horizontal scales (Zhou and Feingold, 2023).

Most studies examine the dependence of cloud susceptibilities on cloud morphology by separating data into cloud scenes associated with different meteorological conditions or precipitation states. These factors co-vary with cloud morphology, which is typically defined by cloud fraction (CF) regime (Gryspeerdt and Stier, 2012; Gryspeerdt et al., 2019; Chen et al., 2025; Hoffmann et al., 2024, 2025; Toll et al., 2019; Glassmeier et al., 2021; Rosenfeld et al., 2019; Zhang et al., 2022). Nevertheless, even within the same type of CF regime, LWP and $\tau_c$ may still exhibit spatial variability, for example due to variations in veil cloud extent in open cells or in cell size distribution within closed cells (Goren et al., 2023; Wood et al., 2018; Zhou and Feingold, 2023). These variations can affect the derived susceptibilities, as shown by Goren et al. (2023) and Zhou and Feingold (2023). Zhou and Feingold (2023), for example, showed that $S_{\mathrm{LWP}}$ in closed cells with smaller horizontal extent can be up to ten times larger than in cells with larger horizontal extent. They attributed these differences to dynamically stronger entrainment-driven evaporation in the smaller cells. Also $S_{A_c}$ has been shown to depend on morphology, as demonstrated by Goren et al. (2023), who found that $S_{A_c}$ can be positively biased by up to 50 % if the spatial distribution of $\tau_c$ within a given $1^\circ \times 1^\circ$ scene is ignored.

Here, we introduce a new method for characterizing cloud morphology that provides a continuous, rather than a discrete, classification. Using this framework, we explore fundamental properties of marine low-level cloud morphologies and calculate cloud albedo, LWP, and CF susceptibilities to $N_d$ conditioned on morphology. Section 2 introduces the ternary morphology approach, Sect. 3 presents the results, and conclusions are given in Sect. 4.

## 2 Data and methods

### 2.1 Data

Satellite observations of marine low-level clouds over the oceans between 60° N–60° S in 2015 were selected for the analysis. The observations were taken from the Moderate Resolution Imaging Spectroradiometer (MODIS) Aqua instrument (Platnick et al., 2016), which provides a nadir resolution of 1 km × 1 km. Scenes were filtered to retain only single layer liquid clouds using the MODIS multilayer flag and cloud phase retrieval. Pixels with sensor zenith angles > 55° or solar zenith angles > 65° were excluded due to retrieval uncertainties (Grosvenor et al., 2018). The satellite retrieved variables used include the corrected reflectance at 0.86 µm, CF (at 5 km × 5 km resolution), LWP, $\tau_c$, and cloud top effective radius, $r_e$. $N_d$ was derived from $r_e$ and $\tau_c$ following Grosvenor et al. (2018). The cloud-core LWP was also computed, defined as the mean LWP of the 10 % of pixels with the highest LWP within a scene.

To diagnose cloud morphology, one must define an area large enough to capture the relevant morphological scales. For marine low level clouds, morphology scales range from a few tens of kilometers up to about 200 km (Zhou et al., 2021). Following this, the cloud properties of the filtered scenes were gridded onto a uniform $2^\circ \times 2^\circ$ latitude–longitude grid, selected to avoid sampling areas too small to represent the mesoscale cloud morphology. Only scenes with CF > 40 % were used in the analysis to avoid broken cloud regimes with their attendant retrieval uncertainties (Choudhury and Goren, 2025; Grosvenor et al., 2018; Wolters et al., 2010). This criterion removes broken cloud regimes with low CF, such as shallow cumulus, sugar, and gravel (Stevens et al., 2020). Figure A1 shows the occurrence of the scenes included in the analysis, which are accordingly found mainly in the stratocumulus regions where closed cells, open cells, and other types of mesoscale cellular convection are common and have relatively higher CF (Muhlbauer et al., 2014). $A_c$ was calculated following the approach of Schneider and Dickinson (1976):

$$A_c = \frac{A_{\text{all-sky}} - A_{\text{clear-sky}}(1 - \mathrm{CF})}{\mathrm{CF}} \tag{1}$$

where $A_{\text{all-sky}}$ and $A_{\text{clear-sky}}$ were obtained from the Clouds and the Earth's Radiant Energy System (CERES) aboard Aqua (Loeb et al., 2005), and gridded to $2^\circ \times 2^\circ$ to match the gridded MODIS data. CF was obtained from MODIS Aqua (Platnick et al., 2016).

Large eddy simulation (LES) output was taken from Goren et al. (2019). The simulations were performed with the System for Atmospheric Modeling (SAM) LES model (Khairoutdinov and Randall, 2003) and were designed to represent a closed-to-open cell transition event observed over the northeast Atlantic Ocean. A full description of the model setup and the simulated case is provided in Goren et al. (2019).

### 2.2 Methods

#### 2.2.1 Ternary diagram

A ternary diagram is a triangular graph used to visualize the proportions of three components in a mixture, where each

corner of the triangle represents 100 % of one component and any point inside represents the relative contributions of all three, which must sum to 100 %. In this study, the three components are the percentages of cloudy pixels in three $\tau_c$ classes: thin ($\tau_c < 7$), intermediate ($7 \leq \tau_c < 12$), and thick ($\tau_c \geq 12$). The partitioning of $\tau_c$ among the three components was done by counting the pixels in each $2^\circ \times 2^\circ$ scene whose retrieved $\tau_c$ falls into each of the three classes, then normalizing by the total number of pixels with a valid $\tau_c$ in the entire scene. Each scene can therefore be represented as a single point in the ternary diagram corresponding to a unique fractional composition of $\tau_c$, which exhibits a unique morphology (see examples in Fig. 1).

The ternary space was discretized into evenly sized bins, each representing a unique $\tau_c$ morphology. $2^\circ \times 2^\circ$ scenes were assigned to a corresponding morphology bin within the ternary space, and microphysical statistical properties were computed for each bin. Bins containing fewer than 25 scenes were excluded from the analysis and are shown as NaN.

The $\tau_c$ class thresholds are defined on physical grounds, based on fundamental radiative transfer considerations: at $\tau_c \approx 7$, $A_c$ transitions from an approximately linear to a more logarithmic dependence on $\tau_c$, and beyond $\tau_c \approx 12$, any further increase in $\tau_c$ produces only minimal additional brightening of $A_c$. We also tested $\tau_c$ thresholds of 5 and 10 to align with the common definition of thin clouds as those having $\tau_c < 5$ (McCoy et al., 2023; Wood et al., 2018; Choudhury and Goren, 2024). The results did not change the key findings, and the main difference was a shift in the distribution of scenes within the ternary space.

### 2.2.2 Decomposing cloud susceptibilities

The ternary framework allows us to estimate cloud susceptibilities to $N_d$, conditioned on $\tau_c$ morphology. It should be emphasized that the ternary binning does not fix $\tau_c$ or other cloud properties within each morphology bin, as each bin retains natural variability in $N_d$, LWP, $\tau_c$, $A_c$, and CF. This is evident, for example, in the difference between the LWP of cloud cores and that of the entire scene (Fig. 3c and d). Sensitivity tests in which the bin size was increased to allow greater variability in cloud properties within each bin did not affect the results. Transitions between morphology bins could have a stronger albedo response, such as in the case of transitions between closed and open cells (Goren and Rosenfeld, 2014; Watson-Parris et al., 2021), however these are temporally dependent (Goren et al., 2019) and not considered here.

A commonly used approach to estimate $S_{LWP}$ from satellite observations is to regress $\mathrm{d}\ln\mathrm{LWP}$ on $\mathrm{d}\ln N_d$. However, when LWP and $N_d$ are calculated under the adiabatic assumption using the satellite retrieved $\tau_c$ and $r_e$ (Szczodrak et al., 2001), changes in $r_e$ are expected to produce a linear sensitivity of $-0.4$ between $\mathrm{d}\ln\mathrm{LWP}$ and $\mathrm{d}\ln N_d$, assuming constant $\tau_c$ (Gryspeerdt et al., 2019). This effect was found to dominate $S_{LWP}$ in our analysis (Fig. A2) because the variability in $\tau_c$ within each ternary bin is relatively small, as each bin is constrained by a $\tau_c$ class composition. To avoid this bias, $S_{LWP}$ was calculated by subtracting the theoretical approximation of $S_{A_c}$ (Platnick and Twomey, 1994; Twomey, 1991) from the satellite derived $S_{net}$. The residual is assumed to be primarily attributable to $S_{LWP}$, as shown below.

$S_{net}$ (the in-cloud albedo susceptibility) can be written using the chain rule (Bellouin et al., 2020) as:

$$S_{net} \equiv \frac{\mathrm{d}\ln A_c}{\mathrm{d}\ln N_d} = \frac{\partial \ln A_c}{\partial \ln N_d}\bigg|_{LWP} + \frac{\partial \ln A_c}{\partial \ln \mathrm{LWP}}\bigg|_{N_d} \frac{\mathrm{d}\ln\mathrm{LWP}}{\mathrm{d}\ln N_d}. \quad (2)$$

Here, $S_{net}$ is defined as the susceptibility of in-cloud albedo to $N_d$, and therefore does not include adjustments in CF. This differs from formulations based on scene-mean albedo (Bellouin et al., 2020), where CF changes contribute an additional term. The first term on the right hand side represents the cloud albedo response to $N_d$, $S_{A_c}$ (Twomey, 1991). Using the cloud albedo theoretical approximation (Twomey, 1991; Platnick and Twomey, 1994),

$$S_{A_c} \equiv \frac{\partial \ln A_c}{\partial \ln N_d}\bigg|_{LWP} = \frac{1}{3}(1 - A_c), \quad (3)$$

where $A_c$ is the in-cloud albedo of each $2^\circ \times 2^\circ$ scene. $S_{A_c}$ is then averaged to obtain the mean $S_{A_c}$ within each morphology bin, $\overline{S}_{A_c}$.

$\frac{\partial \ln A_c}{\partial \ln \mathrm{LWP}}\Big|_{N_d}$ in Eq. (2) represents how changes in LWP modify $A_c$. Because $A_c$ depends primarily on $\tau_c$, and $\tau_c \propto \mathrm{LWP}^{5/6} N_d^{1/3}$ (Platnick and Twomey, 1994; Twomey, 1991), we can write:

$$\gamma \equiv \frac{\partial \ln A_c}{\partial \ln \mathrm{LWP}}\bigg|_{N_d} = \frac{5}{6}\frac{\partial \ln A_c}{\partial \ln \tau_c}\bigg|_{N_d} = \frac{5}{6}(1 - A_c) \quad (4)$$

so that Eq. (2) becomes:

$$S_{net} \equiv \frac{\mathrm{d}\ln A_c}{\mathrm{d}\ln N_d} = S_{A_c} + \gamma \frac{\mathrm{d}\ln\mathrm{LWP}}{\mathrm{d}\ln N_d}. \quad (5)$$

For each morphology bin, we estimate $S_{net}$ by regressing the observed $\ln A_c$ on $\ln N_d$ using all scenes within that bin. For consistency with $S_{A_c}$, we use the bin mean in-cloud albedo, $\overline{A_c}$ in $\gamma$, so that $\overline{\gamma} = \frac{5}{6}(1 - \overline{A_c})$. Evaluating Eq. (2) at each morphology bin gives:

$$S_{net} = \overline{S}_{A_c} + \overline{\gamma} \frac{\mathrm{d}\ln\mathrm{LWP}}{\mathrm{d}\ln N_d}. \quad (6)$$

Solving for $S_{LWP}$ yields $S_{LWP}$ per morphology bin:

$$S_{LWP} \equiv \frac{\mathrm{d}\ln\mathrm{LWP}}{\mathrm{d}\ln N_d} = \frac{S_{net} - \overline{S}_{A_c}}{\overline{\gamma}}. \quad (7)$$

$S_{LWP}$ may implicitly include the influence of CF adjustments on the sampled in-cloud LWP, consistent with previous LWP adjustment studies (Gryspeerdt et al., 2019; Possner et al., 2020; Mülmenstädt et al., 2024).

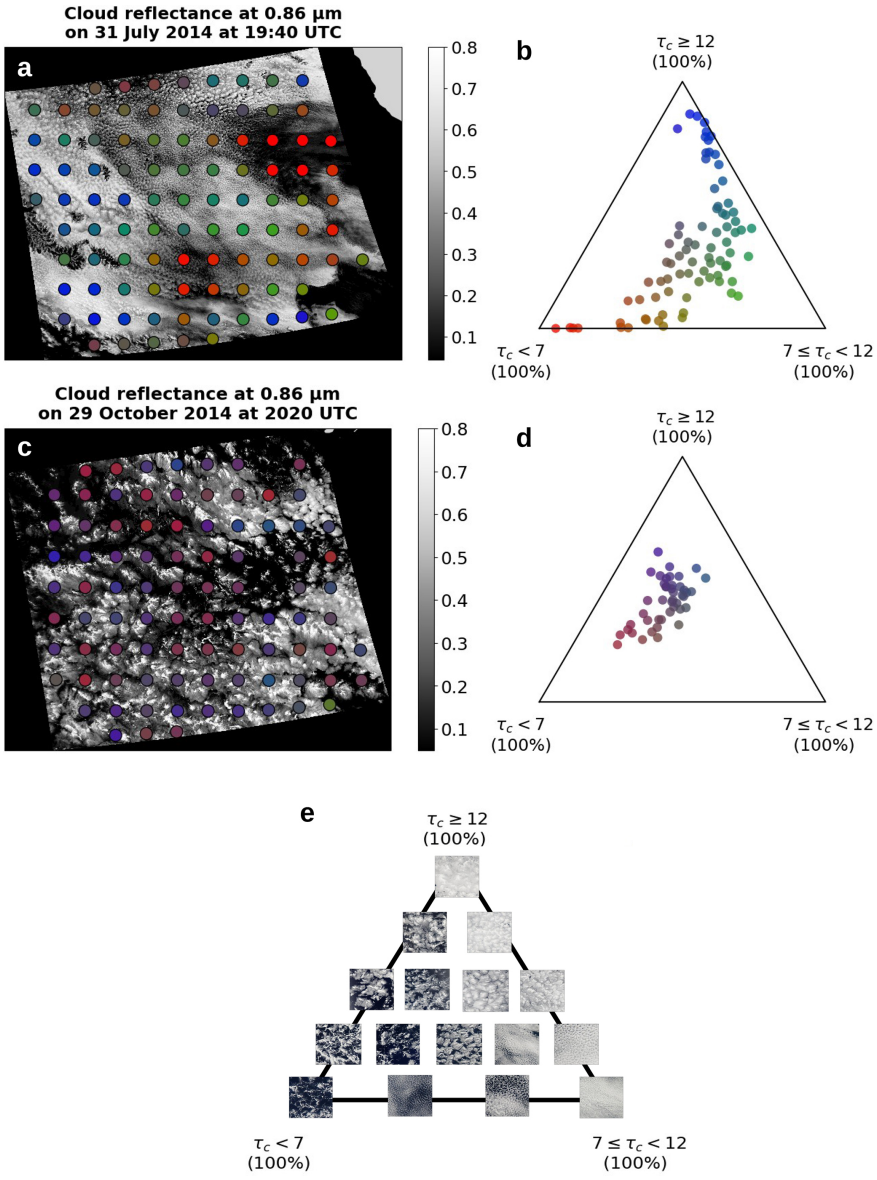


**Figure 1.** Examples of cloud morphology across the ternary morphology space. A ternary diagram illustrates the relative contributions of three components to a system, where each point represents the fractional contributions of the three components and each corner corresponds to 100 % of one component. The ternary corners are defined by $\tau_c$ classes: thin clouds ($\tau_c < 7$), intermediate clouds ($7 \leq \tau_c < 12$), and thick clouds ($\tau_c \geq 12$). Panels **(a)** and **(c)** show MODIS reflectance at 0.86 µm, illustrating different cloud morphologies over the Pacific ocean East of North and South America, respectively. Each MODIS swath image is approximately 2330 km wide and 2100 km long. Panels **(b)** and **(d)** show the ternary diagram populated with $2° \times 2°$ scenes from the corresponding MODIS swaths in **(a)** and **(c)**. Colored points represent the fractional contributions of the three $\tau_c$ classes as an RGB composite, with red corresponding to $\tau_c < 7$, green to $7 \leq \tau_c < 12$, and blue to $\tau_c \geq 12$. Panel **(e)** shows MODIS true-color scenes illustrating common cloud morphologies across the ternary space. The scenes were selected such that their ternary composition matches their position within the ternary diagram.

$S_{CF}$, defined as the CF susceptibility to $N_d$, was calculated by regressing the observed ln(CF) on ln($N_d$) for each ternary bin. Explicitly disentangling $S_{LWP}$ from $S_{CF}$ is challenging, as it is not uniquely defined how spatially heterogeneous changes in LWP should be attributed to variations in CF (Hoffmann et al., 2025).

## 3 Results

### 3.1 Examples of cloud morphology represented in ternary space

Figure 1a and c show two MODIS swaths containing different cloud morphologies. Figure 1b and d show the corre-

sponding $2° \times 2°$ scenes from these swaths mapped onto the ternary diagram. Homogeneous scenes, in which the cellular structure is weakly expressed, are located near the corners of the ternary diagram, whereas inhomogeneous scenes with a more pronounced cellular structure are positioned away from the corners due to their mixed $\tau_c$ composition.

The cloud morphology can be seen to vary with CF, cell horizontal scale (large vs. small cells), and cloud reflectance, which can differ among cells of similar size. This means that cells with similar horizontal scales can be associated with different morphologies when their scene mean cloud albedo (or $\tau_c$) is different. This extends the study of Zhou and Feingold (2023), which focused on classifying cell morphology by size, by additionally highlighting the role of $\tau_c$ variability across cells of similar size.

The morphologies in Fig. 1a are predominantly overcast, with homogeneous scenes appearing either as thin stratus layers (red points in Fig. 1a and b) or as thick closed cells (blue points in Fig. 1a and b). Between these lie heterogeneous morphologies with stronger contrast between cell cores and their surrounding clouds, reflecting a mixture of $\tau_c$ classes.

Figure 1c shows scenes of broken CF and closed cells with larger horizontal extent. These scenes typically correspond to precipitating clouds composed of thick cores ($\tau_c \geq 12$ class) surrounded by a relatively large fraction of thin clouds ($\tau_c < 7$ class) (Wood et al., 2018; O et al., 2018), with only a limited contribution from the moderate $\tau_c$ class ($7 \leq \tau_c < 12$). This distinct morphology places these scenes farther toward the left side of the ternary diagram.

## 3.2 Occurrence of cloud morphologies

### 3.2.1 Observations

Figure 2a shows the 2015 distribution of scenes within the ternary morphology space. The most frequent morphologies are composed of a mixture of homogeneous optically thick and homogeneous optically thin clouds, with a relatively small contribution from the intermediate $\tau_c$ class. This implies that most of the variability in scene morphology arises from changes in the relative contributions of the thick and thin $\tau_c$ classes, whereas the fractional contribution of the intermediate $\tau_c$ class is relatively low. Such a mixtures of $\tau_c$ classes characterize active convective cores that coexist with thin clouds diverging from the cloud tops (Wood et al., 2018; Choudhury and Goren, 2024; O et al., 2018). The example in Fig. 1c and d shows this morphological type, consisting primarily of open cells and disorganized mesoscale cellular convection (Muhlbauer et al., 2014). Similar spatial variability in LWP has been used to distinguish disorganized mesoscale cellular convection from closed and open cells, and from stratus cloud layers with no cellular structure (Wood and Hartmann, 2006; Muhlbauer et al., 2014).

The least frequent morphologies correspond to homogeneous scenes with intermediate $\tau_c$. Interestingly, the scene-mean $\tau_c$ of all sampled scenes falls within this $\tau_c$ class, with an average value of approximately 9. This means that scene means often reflect a mixture of thick and thin clouds and are therefore not representative of the underlying $\tau_c$ distribution. Indeed, Goren et al. (2023) showed that relying on the scene-mean $\tau_c$, rather than accounting for its spatial variability, can lead to a substantial bias in $S_{A_c}$. Another less frequent morphology appears near the very left side of the ternary, where scenes are dominated by a mixture of thick and thin clouds, with minimal contribution from the intermediate $\tau_c$ class.

Figure 2b shows the median CF per ternary bin, revealing a clear separation between overcast and broken scenes. This indicates that overcast and broken scenes are associated with different $\tau_c$ morphologies. The highest scene occurrence (Fig. 2a) is found for broken cloud morphologies, consistent with previous studies. These scenes are attributed to the high occurrence of disorganized mesoscale cellular convection (Muhlbauer et al., 2014; Goren et al., 2025). The analysis therefore mainly represents stratocumulus clouds, primarily closed and open cells, disorganized mesoscale cellular convection, and stratus layers with no cellular pattern.

### 3.2.2 Large eddy simulations

Figure 2c and d show the morphology evolution of simulated clouds obtained from a Lagrangian LES of closed cells transitioning to open cells (Goren et al., 2019). The simulated clouds evolve along a morphology trajectory that closely matches the region of highest occurrence in the observations (Fig. 2a). This suggests that most observed scenes lie within the stratocumulus morphology evolution space that the analysis is designed to represent.

The simulated evolution of the cloud morphology also provides insight into key cloud processes. One example is cloud thickening during nighttime at the beginning of the simulation, driven by cloud top radiative cooling (Goren et al., 2019). Another is the diurnal cycle in cloud morphology, evident from the daytime loop feature in Fig. 2c and d. The loop feature shows an increased contribution from the intermediate $\tau_c$ class at the expense of the high $\tau_c$ class during the daytime morphology evolution (Fig. 2c), implying cloud thinning. It is driven by the daytime increase in solar radiation, which leads to cloud thinning and CF reduction (Fig. 2d) through warming and evaporation (Hignett, 1991; Meskhidze et al., 2009). Interestingly, the afternoon cloud thickening follows the same morphological trajectory as the cloud thickening during the previous night, suggesting a preferred evolutionary path. This can explain why the observed cloud morphologies do not span the entire ternary space but instead are concentrated along a preferred region within the morphology space (Fig. 2a). It remains an open question for future study whether a given morphological state can be reached through different paths.

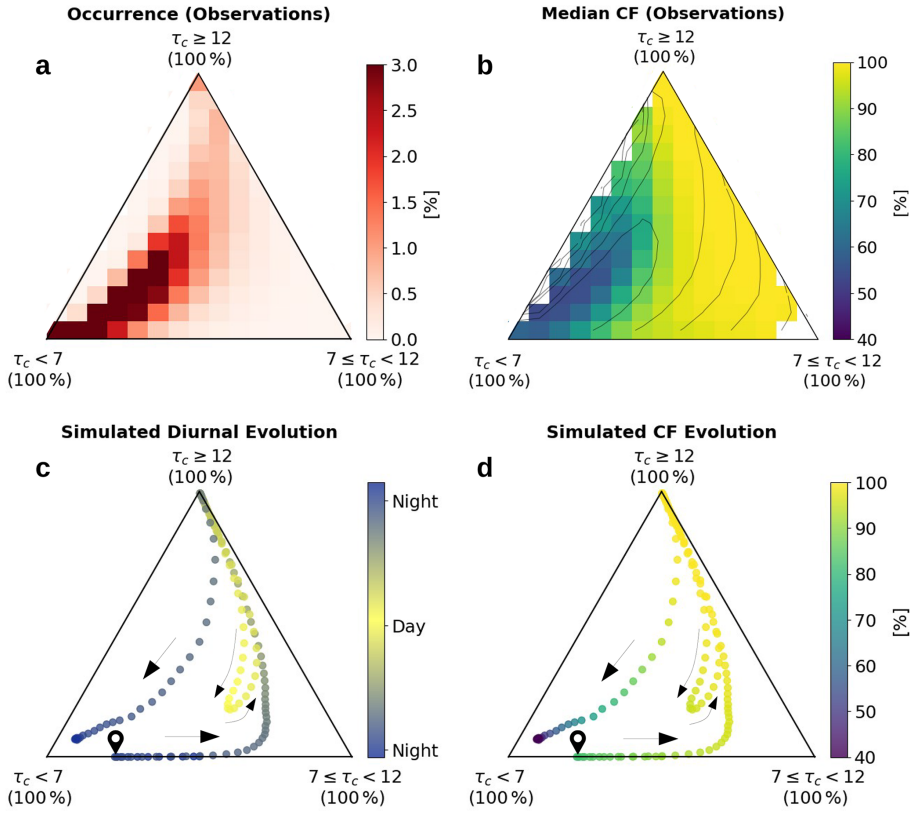


**Figure 2.** Ternary diagrams of scene occurrence and cloud fraction for satellite observations and LES. **(a)** Occurrence of $2° \times 2°$ scenes from one year (2015) of MODIS Aqua observations of marine low clouds having CF $> 40\,\%$. Percentages represent the relative contribution of each morphology bin. **(b)** Median CF for each morphology bin, with contours indicating scene occurrence derived from **(a)**. **(c)** LES simulation of overcast closed cells transitioning to open cells over a 24 h period, with time indicated by the color bar. **(d)** Same as **(c)**, but showing CF. Arrows indicate the direction of the temporal evolution across the ternary space, with the pin icon indicating the beginning of the simulation. The closed-loop represents daytime cloud thinning, with the recovery later in the day overlapping the preceding nighttime trajectory. The simulated rate of change of the morphology can be inferred from the spacing between successive points.

The ternary representation also captures the rapid cloud breakup, indicated by the downward-pointing arrows in Fig. 2c and d. Because cloud breakup occurs concurrently with the development of substantial precipitation (Goren et al., 2019; Rosenfeld et al., 2006), scenes occupying this morphology space are presumably associated with collision and coalescence processes (Wang and Feingold, 2009).

The above demonstrates that the distribution of scenes within the ternary space encodes information about underlying cloud processes, such as cloud thickening, thinning, and collision–coalescence. Satellite observations projected onto the ternary space can therefore provide information about the state of the cloud field, as different regions of the diagram correspond to distinct cloud processes.

### 3.3 Cloud properties across the ternary morphology space

Figure 3 shows the microphysical properties across the ternary morphology space. In morphology bins characterized by low CF (Fig. 2b), $N_d$ is relatively low and $r_e$ exceeds 15 µm (Fig. 3a and b). This suggests that precipitation-driven breakup of overcast clouds could lead to the observed lower CF (Rosenfeld et al., 2006; Stevens et al., 2005; Wang and Feingold, 2009; Goren et al., 2019).

An interesting pattern emerges in the LWP field (Fig. 3c). High LWP extends from the high $\tau_c$ class toward the low $\tau_c$ class (thin clouds), along the left side of the ternary. This pattern is somewhat counterintuitive because one might expect high LWP to extend toward the intermediate $\tau_c$ class. The reason becomes clear in Fig. 3d, which shows the LWP of the cloud cores, defined as the 10 % of pixels with the largest LWP. The core LWP is largest along the left side of the ternary, extending toward the lower $\tau_c$ class, indicating that the cores remain thick while an increasing fraction of surrounding pixels is gradually replaced by thinner clouds. This morphology is characteristic of stratocumulus in a deep boundary layer, where cloud-top divergence creates thin cloud layers at the top of the boundary layer (Wood et al., 2018; O et al., 2018; Goren et al., 2023; Choudhury and

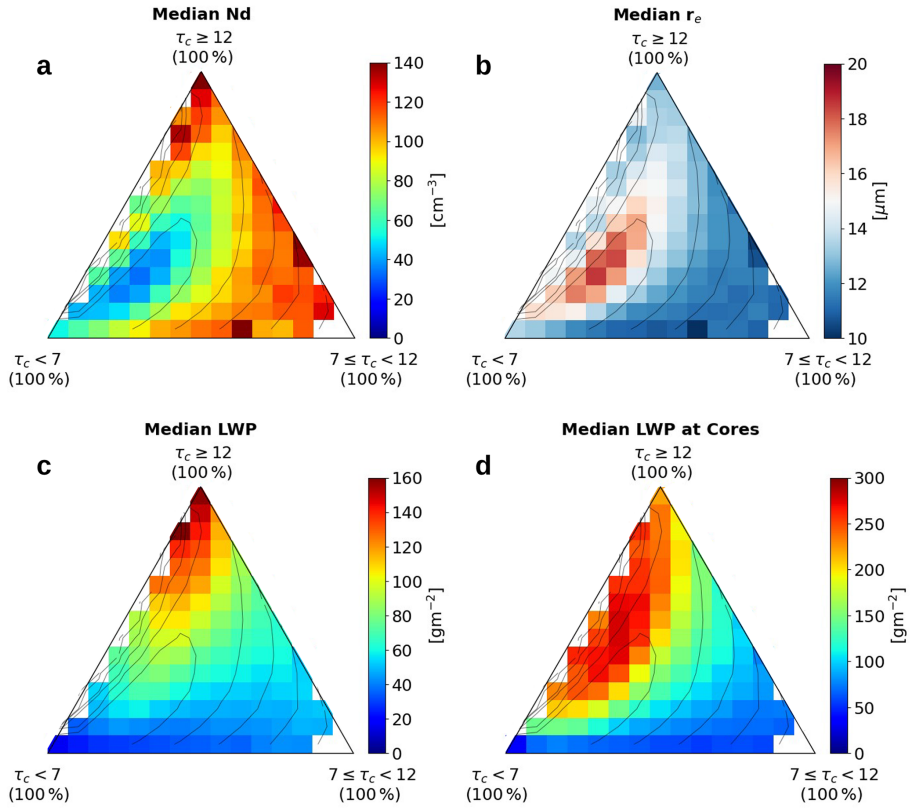


**Figure 3.** Median ternary-bin values of **(a)** $N_d$, **(b)** $r_e$, **(c)** LWP, and **(d)** cloud-core LWP, defined as the mean LWP of the 10 % of pixels with the highest LWP in each scene. Contours indicate scene occurrence, as in Fig. 2b.

Goren, 2024). It reflects a morphological progression associated with the stratocumulus to cumulus transition (Bretherton and Wyant, 1997; Wyant et al., 1997), consistent with the examples in Fig. 1c and d, as well as with the simulated closed to open cloud trajectory (Fig. 2c and d).

At the left corner of the ternary diagram (the $\tau_c < 7$ class), scenes have low LWP. These scenes can be associated with the early stages of stratocumulus formation, typically appearing as an optically thin cloud layer lacking cellular structure (Fig. 1a, red points), or with the late stages of dissipating precipitating cells that leave remnants of thin cloud layers near the top of the boundary layer (Choudhury and Goren, 2024; Wood et al., 2018; O et al., 2018). The simulated morphology evolution further supports that clouds both form and dissipate near the lowest $\tau_c$ class (Fig. 3c and d).

## 3.4 Morphology-conditioned cloud susceptibilities

### 3.4.1 LWP susceptibility

Figure 4a shows that $S_{LWP}$ is negative across the entire ternary space. This contrasts with previous studies that reported both positive and negative $S_{LWP}$, with the positive values attributed to precipitation suppression (Gryspeerdt et al., 2019; Possner et al., 2020). The negative $S_{LWP}$ indicates that entrainment-related evaporation processes dominate across all morphologies, leading to a reduction in LWP as droplet size decreases with increasing $N_d$ (Bretherton et al., 2007; Hoffmann et al., 2025; Pincus and Baker, 1994; Wood, 2007). The strongest $S_{LWP}$ of nearly $-1$ is found in morphology bins where the intermediate $\tau_c$ class is dominant. In these scenes the horizontal cell sizes are relatively small (Fig. 4a), consistent with Zhou and Feingold (2023), who found similarly strong $S_{LWP}$ in nonprecipitating small closed cells.

$S_{LWP}$ weakens (becomes less negative) as the contribution from the intermediate $\tau_c$ class decreases and is replaced by increasing contributions from the lowest and highest $\tau_c$ classes. This partly coincides with an increase in $r_e$ to values close to 15 µm (Fig. 3b), indicating the presence of precipitation (Rosenfeld et al., 2012), and suggests that precipitation suppression contributes to the weakened $S_{LWP}$, but not sufficiently to reverse its sign. Additionally, the dominance of thin cloud layers in these morphologies tends to be associated with more quiescent turbulent conditions (Wood et al., 2018), limiting their ability to entrain free-tropospheric air and thus constraining $S_{LWP}$. Our findings are consistent with Goren et al. (2025), who showed that the positive $S_{LWP}$ reported for precipitating scenes in many inverted-V studies (Gryspeerdt et al., 2019; Mülmenstädt et al., 2024; Glass-

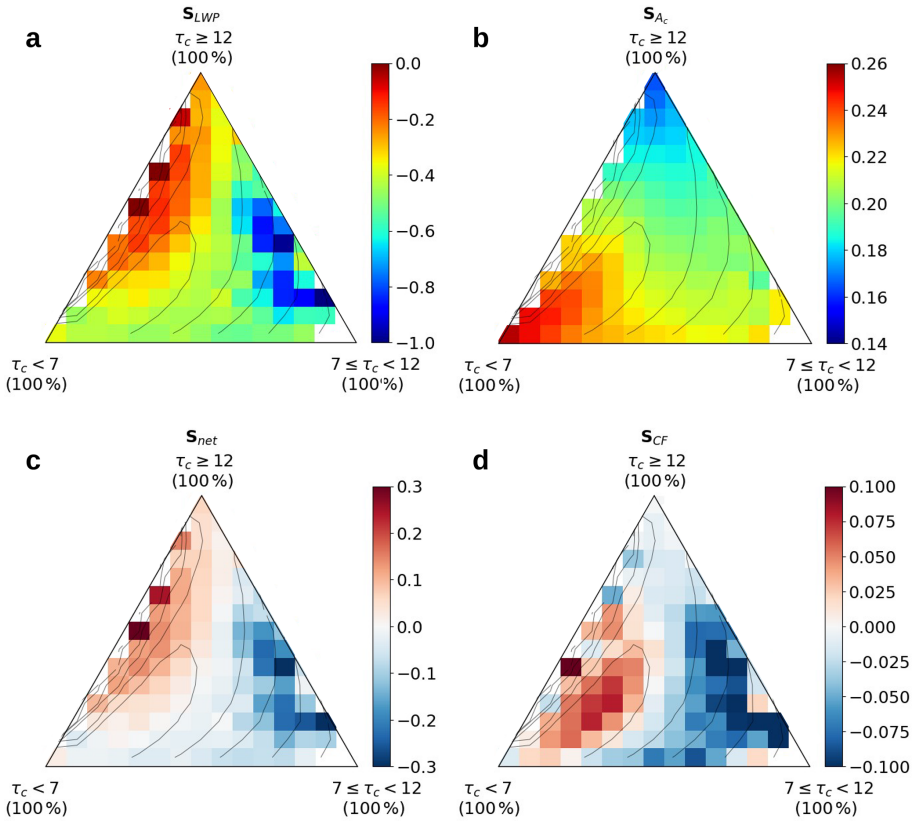


**Figure 4.** Cloud albedo susceptibility to $N_d$ for **(a)** LWP, **(b)** $A_c$ (Twomey effect), **(c)** net cloud albedo, and **(d)** CF. Contours represent scene occurrence, as in Fig. 2b.

meier et al., 2021; Possner et al., 2018) does not necessarily reflect precipitation suppression, but can instead arise as an artifact of aggregated sampling across different cloud morphologies.

The weakest $S_{LWP}$ is found in morphologies composed of a mixture of thick and thin $\tau_c$ classes, with minimal contribution from the intermediate $\tau_c$ class. These morphologies are characterized by relatively large cell sizes (Fig. 1c) and $r_e$ close to or exceeding 15 µm (Fig. 3), indicating mature closed cells approaching breakup (Goren et al., 2022; Choudhury and Goren, 2024). This is consistent with Zhou and Feingold (2023), who reported weak $S_{LWP}$ for the largest cell sizes. In addition to delayed cloud breakup due to the delayed onset of precipitation, the weak $S_{LWP}$ in these morphologies may also arise from differences in entrainment efficiency between thick cloud cores and the surrounding thin clouds (Zhou and Feingold, 2023; Bretherton et al., 2007; Kazil et al., 2017). Additionally, the non-negligible contribution of the highest $\tau_c$ class indicates the presence of thick, dynamically active cores, as evidenced by the large core-LWP (Fig. 1d). These cores likely supply cloud water to the diverging thinner clouds at their tops, which could partially offset LWP losses due to entrainment-driven evaporation, thereby further weakening the negative LWP response.

### 3.4.2 Cloud albedo susceptibility

Figure 4b shows that the strongest $S_{A_c}$ occurs in the lowest $\tau_c$ class and extends toward the top corner, towards the highest $\tau_c$ class, with the largest gradient along the left side of the ternary diagram. This is consistent with the theoretical approximation of $S_{A_c}$ (Platnick and Twomey, 1994; Twomey, 1991), which predicts the largest susceptibility for scenes with the lowest $A_c$ (see Fig. A3 for the distribution of $A_c$ across the ternary space).

### 3.4.3 Net albedo susceptibility

Figure 4c shows a strong dependence of $S_{net}$ on cloud morphology. $S_{net}$ is negative in scenes dominated by intermediate $\tau_c$ classes and shifts toward positive values as the morphology becomes dominated by a mixture of thick and thin $\tau_c$ classes. The similarity between the morphological dependence of $S_{net}$ and $S_{LWP}$ (Fig. 4a) arises because $S_{A_c}$ (Fig. 4b) exhibits relatively little variability compared to $S_{LWP}$. This indicates that $S_{net}$ is primarily controlled by $S_{LWP}$. The strong influence of LWP adjustments on the net albedo response can also be shown theoretically (Feingold and Siebert, 2009).

The strongest negative $S_{net}$ is found in scenes dominated by the intermediate $\tau_c$ class, where $S_{LWP}$ outweighs the

relatively strong in-cloud albedo response associated with the Twomey effect, $S_{A_c}$ (Fig. 4b). This is consistent with Zhang et al. (2022), who found that thicker non-precipitating clouds, which likely correspond to the intermediate $\tau_c$ class here, exhibit cloud darkening. The strongest positive $S_{net}$, on the other hand, occurs where $S_{LWP}$ is weakest, that is, least negative (Fig. 4a), allowing the Twomey brightening ($S_{A_c}$) to enhance $A_c$ without being substantially offset by the LWP adjustments.

Both the strongest negative and the strongest positive $S_{net}$ are associated with the least frequent morphologies (Fig. 2a), whereas for the most frequent morphologies, $S_{LWP}$ and $S_{A_c}$ approximately balance each other, resulting in $S_{net}$ near zero. As a result, the global mean $S_{net}$ is relatively small, with a value of approximately $0.015 \pm 0.007$. The uncertainty of the weighted mean slope was estimated from the variability across bin-specific slopes, accounting for the effective sample size. A substantial offset of the Twomey induced brightening by LWP adjustments has also been reported in previous studies (Prabhakaran et al., 2023; Toll et al., 2019; Diamond et al., 2020). It should be noted that the global mean $S_{net}$ reflects the morphological occurrence of the year analyzed here. A future study will explore whether there are interannual differences in morphological occurrence, for example during El Nino years, as well as across seasons and regions.

### 3.4.4 Cloud cover susceptibility

The LWP and $A_c$ susceptibility analysis focused on in-cloud changes, without considering changes in CF. Here, we further examine $S_{CF}$ (Fig. 4d). Positive $S_{CF}$ is found in precipitating scenes, as indicated by $r_e > 15\,\mu m$ (Fig. 3b), consistent with studies reporting a positive relationship between CF and $N_d$ (Rosenfeld et al., 2019; Chen et al., 2014; Wall et al., 2022; Goren and Rosenfeld, 2014). Since stratocumulus breakup is driven by the formation of precipitation (Goren et al., 2019, 2022; Yamaguchi et al., 2017), the positive $S_{CF}$ reflects the effect of increased $N_d$ in slowing precipitation formation, which slows down the reduction of CF.

Negative values of $S_{CF}$, by contrast, are found in non-precipitating scenes ($r_e < 15\,\mu m$). These scenes are composed primarily of the intermediate $\tau_c$ class, where $S_{LWP}$ is strong and negative (Fig. 4a). This suggests that the negative strong $S_{LWP}$ drives the negative $S_{CF}$. The scene-mean LWP in these morphology bins is relatively low (Fig. 3c), such that evaporation of cloud water associated with the strong $S_{LWP}$ presumably leads to cloud dissipation and, consequently, a reduction in CF. We assume that the reduction in CF is associated with the thinner clouds at the edges of the cells (see examples in Fig. 1e), consistent with the assumptions in Goren and Rosenfeld (2014). The daytime cloud thinning and the associated small reduction in CF shown in Fig. 2c and d correspond to the negative $S_{CF}$ shown in in Fig. 4d, consistent with the reported daytime decrease in CF (Hignett, 1991; Meskhidze et al., 2009). Weak negative $S_{CF}$ are found where scenes are dominated by the thickest $\tau_c$ class. In these scenes, clouds are thick and have high LWP, so changes in LWP do not substantially affect scene CF.

## 4 Conclusions

We have introduced a new method for defining stratocumulus cloud morphologies using a ternary diagram. The ternary is composed of three $\tau_c$ classes and provides a continuous morphology space, in contrast to commonly used discrete cloud morphology regime classifications (Wood and Hartmann, 2006; Muhlbauer et al., 2014; Erfani and Hosseinpour, 2025; Wu et al., 2025; Yuan et al., 2020; Geiss et al., 2024). Using one year of satellite observations, we quantify the occurrence of scenes across the morphology space, revealing a preference for a confined range of morphologies. Complemented by LES, we show that cloud morphology evolution follows a preferred path across the ternary morphology space, explaining why most observations fall within a confined range of morphologies. The ternary framework also reveals insights into cloud processes associated with morphology changes, including cloud thickening, the diurnal cycle, and cloud breakup driven by precipitation. This suggests that the ternary encodes information about cloud processes that can be inferred from instantaneous satellite snapshots when projected into this space. The analysis also shows that scenes are often composed of mixtures of thick and thin clouds, making scene-mean values of spatially varying cloud properties, such as LWP and $\tau_c$, not representative of the underlying cloud field. Using these means can therefore introduce biases in quantities that rely on these mean values (Goren et al., 2023).

The ternary framework allows us to estimate the susceptibilities of LWP, CF, and $A_c$ to $N_d$, conditioned on cloud morphology. $S_{LWP}$ is found to be negative across all morphologies, including in precipitating ones, in contrast to studies that have reported positive $S_{LWP}$ and attributed it to precipitation suppression (Dipu et al., 2022; Glassmeier et al., 2021; Gryspeerdt et al., 2019; Mülmenstädt et al., 2024; Possner et al., 2020). Our results support Goren et al. (2025), who showed that the positive $S_{LWP}$ inferred from inverted-V joint histograms of LWP and $N_d$ arises as an artifact of aggregated sampling across different cloud morphologies. The strength of the negative $S_{LWP}$ is found to depend on morphology, even for non-precipitating clouds, consistent with Zhou and Feingold (2023). Earlier studies, however, often reported a bulk approximation for $S_{LWP}$ (Gryspeerdt et al., 2019; Glassmeier et al., 2021; Possner et al., 2020), thereby not capturing the morphology-dependent variability. Detecting a morphology-dependent $S_{LWP}$ was possible by treating morphology as an observed variable, which also reduces confounding aerosol–meteorology co-variability that has been suggested to produce spurious negative values of $S_{LWP}$ (Goren et al., 2025; Mülmenstädt et al., 2024).

$S_{CF}$ is found to be positive in precipitating scenes, presumably because increased $N_d$ delays precipitation and, consequently, cloud breakup (Goren et al., 2019; Wang and Feingold, 2009; Yamaguchi et al., 2017). On the other hand, in non-precipitating scenes with low LWP, $S_{CF}$ is found to be negative, presumably because the strong negative $S_{LWP}$ in these scenes reduces CF through entrainment-related evaporation processes. It should be noted that scenes with negative $S_{CF}$ occur less frequently than those with positive $S_{CF}$, indicating that positive $S_{CF}$ dominates the global signal.

The net in-cloud albedo susceptibility, $S_{net}$, is the most relevant for the radiation budget because it includes the combined contributions of $S_{A_c}$ and $S_{LWP}$. $S_{net}$ is found to vary between −0.3–0.3 depending on cloud morphology, largely modulated by the strong control of $S_{LWP}$. This implies that, in some morphological regimes, Twomey-induced brightening is offset by LWP adjustments, consistent with findings from previous studies (Prabhakaran et al., 2023; Toll et al., 2019; Diamond et al., 2020). Here, we further show that this offset can fully cancel, and even exceed, the Twomey-induced brightening, leading to a net negative effect. When averaged over all morphologies, $S_{net}$ is overall small ($0.015 \pm 0.007$), as it is dominated by the most frequently occurring morphologies, which have lower $S_{net}$. This implies that a global 10 % increase in $N_d$ would result in an increase in cloud albedo of approximately $0.15 \pm 0.07$ %, not accounting for changes in CF. The analysis suggests that marine cloud brightening would need to target morphologies with positive $S_{net}$ and rely on persistently positive $S_{CF}$ to be effective. The results also have implications for estimates of aerosol–cloud radiative forcing, which should account for morphology-weighted contributions.

## Appendix A: Additional figures

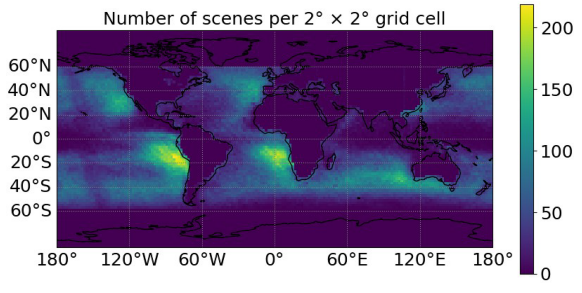


**Figure A1.** Number of scenes per 2° × 2° grid cell used in the analysis. It can be seen that most scenes derive from the stratocumulus regions in the eastern subtropical oceans.

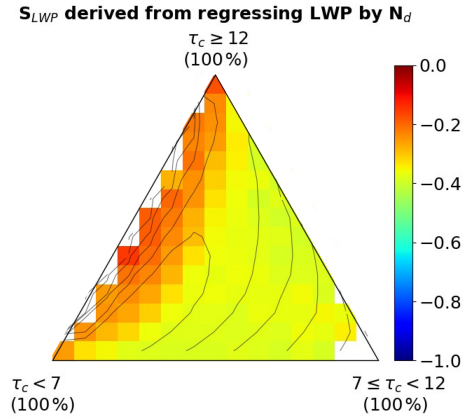


**Figure A2.** LWP susceptibility derived from the regression between ln LWP and ln $N_d$ within each ternary bin. Contours represent scene occurrence, as in Fig. 2b.

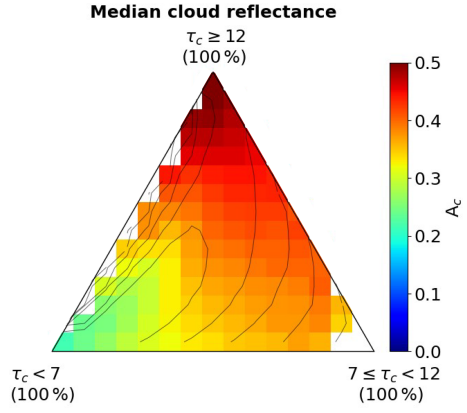


**Figure A3.** Median ternary-bin values of $A_c$. Contours indicate scene occurrence, as in Fig. 2b.

**Data availability.** All data sets used in this work are open source. The MODIS aqua cloud products are available from the Atmosphere Archive and Distribution System (LAADS) Distributed Active Archive Center (DAAC): https://ladsweb.modaps.eosdis.nasa.gov/archive/allData/61/MOD06_L2/ (last access: 30 April 2026). CERES radiation data can be accessed at https://ceres.larc.nasa.gov/data/ (last access: 30 April 2026). ERA5 pressure level data were obtained from Copernicus Climate Change Service (C3S) Climate Data Store accessible at https://cds.climate.copernicus.eu/ (last access: 30 April 2026).

**Author contributions.** TG conceptualized the research idea, carried out the study, and wrote the manuscript. GC preprocessed the datasets used in the analysis. All authors contributed to discussions and to the writing of the manuscript.

**Competing interests.** At least one of the (co-)authors is a member of the editorial board of *Atmospheric Chemistry and Physics*. The peer-review process was guided by an independent editor, and the authors also have no other competing interests to declare.



**Acknowledgements.** This work has received funding from the Israel Science Foundation (grant no. 3171/24), the United States – Israel Binational Science Foundation (BSF) (grant number 2024152) and the German Research Foundation (Deutsche Forschungsgemeinschaft, DFG; grant number 524386224). Graham Feingold acknowledges support from the NOAA Earth's Radiation Budget Grant #03-01-07-001.

**Financial support.** This research has been supported by the United States – Israel Binational Science Foundation (grant no. 2024152), the Israel Science Foundation (grant no. 3171/24), the Deutsche Forschungsgemeinschaft (grant no. 524386224), and NOAA Earth's Radiation Budget (grant no. 03-01-07-001).

**Review statement.** This paper was edited by Anna Possner and reviewed by two anonymous referees.

## References

Ackerman, A. S., Kirkpatrick, M. P., Stevens, D. E., and Toon, O. B.: The impact of humidity above stratiform clouds on indirect aerosol climate forcing, Nature, 432, 1014–1017, https://doi.org/10.1038/nature03174, 2004.

Albrecht, B. A.: Aerosols, cloud microphysics, and fractional cloudiness, Science, 245, 1227–1230, 1989.

Bellouin, N., Quaas, J., Gryspeerdt, E., Kinne, S., Stier, P., Watson-Parris, D., Boucher, O., Carslaw, K. S., Christensen, M., Daniau, A. L., Dufresne, J.-L., Feingold, G., Fiedler, S., Forster, P., Gettelman, A., Haywood, J. M., Lohmann, U., Malavelle, F., Mauritsen, T., McCoy, D. T., Myhre, G., Mülmenstädt, J., Neubauer, D., Possner, A., Rugenstein, M., Sato, Y., Schulz, M., Schwartz, S. E., Sourdeval, O., Storelvmo, T., Toll, V., Winker, D., and Stevens, B.: Bounding global aerosol radiative forcing of climate change, Rev. Geophys., 58, e2019RG000660, https://doi.org/10.1029/2019RG000660, 2020.

Bretherton, C. S. and Wyant, M. C.: Moisture transport, lower-tropospheric stability, and decoupling of cloud-topped boundary layers, J. Atmos. Sci., 54, 148–167, 1997.

Bretherton, C. S., Blossey, P. N., and Uchida, J.: Cloud droplet sedimentation, entrainment efficiency, and subtropical stratocumulus albedo, Geophys. Res. Lett., 34, L03813, https://doi.org/10.1029/2006GL027648, 2007.

Chen, Y.-C., Christensen, M. W., Stephens, G. L., and Seinfeld, J. H.: Satellite-based estimate of global aerosol–cloud radiative forcing by marine warm clouds, Nat. Geosci., 7, 643–646, https://doi.org/10.1038/ngeo2214, 2014.

Chen, Y.-S., Prabhakaran, P., Hoffmann, F., Kazil, J., Yamaguchi, T., and Feingold, G.: Magnitude and timescale of liquid water path adjustments to cloud droplet number concentration perturbations for nocturnal non-precipitating marine stratocumulus, Atmos. Chem. Phys., 25, 6141–6159, https://doi.org/10.5194/acp-25-6141-2025, 2025.

Choudhury, G. and Goren, T.: Thin clouds control the cloud radiative effect along the Sc-Cu transition, J. Geophys. Res.-Atmos., 129, e2023JD040406, https://doi.org/10.1029/2023JD040406, 2024.

Choudhury, G. and Goren, T.: Sampling bias from satellite retrieval failures of cloud properties and its implications for aerosol-cloud interactions, Geophys. Res. Lett., 52, e2025GL115429, https://doi.org/10.1029/2025GL115429, 2025.

Davis, A., Marshak, A., Cahalan, R., and Wiscombe, W.: The Landsat scale break in stratocumulus as a three-dimensional radiative transfer effect: implications for cloud remote sensing, J. Atmos. Sci., 54, 241–260, 1997.

Diamond, M. S., Director, H. M., Eastman, R., Possner, A., and Wood, R.: Substantial cloud brightening from shipping in subtropical low clouds, AGU Advances, 1, e2019AV000111, https://doi.org/10.1029/2019AV000111, 2020.

Dipu, S., Schwarz, M., Ekman, A. M., Gryspeerdt, E., Goren, T., Sourdeval, O., Mülmenstädt, J., and Quaas, J.: Exploring satellite-derived relationships between cloud droplet number concentration and liquid water path using a large-domain large-eddy simulation, Tellus B, 74, 176–188, https://doi.org/10.16993/tellusb.27, 2022.

Eastman, R., McCoy, I. L., Schulz, H., and Wood, R.: A survey of radiative and physical properties of North Atlantic mesoscale cloud morphologies from multiple identification methodologies, Atmos. Chem. Phys., 24, 6613–6634, https://doi.org/10.5194/acp-24-6613-2024, 2024.

Erfani, E. and Hosseinpour, F.: A novel approach for reliable classification of marine low cloud morphologies with vision–language models, Atmosphere-Basel, 16, 1252, https://doi.org/10.3390/atmos16111252, 2025.

Feingold, G. and Siebert, H.: Cloud–aerosol interactions from the micro to the cloud scale, in: Clouds in the Perturbed Climate System: Their Relationship to Energy Balance, Atmospheric Dynamics, and Precipitation, edited by: Heintzenberg, J. and Charlson, R. J., MIT Press, Cambridge, Massachusetts, 319–338, https://doi.org/10.7551/mitpress/9780262012874.003.0014, 2009.

Forster, P., Storelvmo, T., Armour, K., Collins, W., Dufresne, J.-L., Frame, D., Lunt, D., Mauritsen, T., Palmer, M., Watanabe, M., Wild, M., and Zhang, H.: Chapter 7: The Earth's energy budget, climate feedbacks, and climate sensitivity, https://doi.org/10.25455/wgtn.16869671, 2021.

Geiss, A., Christensen, M. W., Varble, A. C., Yuan, T., and Song, H.: Self-supervised cloud classification, Artificial Intelligence for the Earth Systems, 3, e230036, https://doi.org/10.1175/AIES-D-23-0036.1, 2024.

Glassmeier, F., Hoffmann, F., Johnson, J. S., Yamaguchi, T., Carslaw, K. S., and Feingold, G.: Aerosol-cloud-climate cooling overestimated by ship-track data, Science, 371, 485–489, 2021.

Goren, T. and Rosenfeld, D.: Decomposing aerosol cloud radiative effects into cloud cover, liquid water path and Twomey components in marine stratocumulus, Atmos. Res., 138, 378–393, https://doi.org/10.1016/j.atmosres.2013.12.008, 2014.

Goren, T., Kazil, J., Hoffmann, F., Yamaguchi, T., and Feingold, G.: Anthropogenic air pollution delays marine stratocumulus breakup to open cells, Geophys. Res. Lett., 46, 14135–14144, 2019.

Goren, T., Feingold, G., Gryspeerdt, E., Kazil, J., Kretzschmar, J., Jia, H., and Quaas, J.: Projecting stratocumulus transitions on the albedo–cloud fraction relationship reveals linearity of albedo to droplet concentrations, Geophys. Res. Lett., 49, e2022GL101169, https://doi.org/10.1029/2022GL101169, 2022.

Goren, T., Sourdeval, O., Kretzschmar, J., and Quaas, J.: Spatial aggregation of satellite observations leads to an overestimation of the radiative forcing due to aerosol-cloud interactions, Geophys. Res. Lett., 50, e2023GL105282, https://doi.org/10.1029/2023GL105282, 2023.

Goren, T., Choudhury, G., Kretzschmar, J., and McCoy, I.: Covariability drives the inverted-V sensitivity between liquid water path and droplet concentrations, Atmos. Chem. Phys., 25, 3413–3423, https://doi.org/10.5194/acp-25-3413-2025, 2025.

Grosvenor, Sourdeval, O., Zuidema, P., Ackerman, A., Alexandrov, M. D., Bennartz, R., Boers, R., Cairns, B., Chiu, J. C., Christensen, M., Deneke, H., Diamond, M., Feingold, G., Fridlind, A., Hünerbein, A., Knist, C., Kollias, P., Marshak, A., McCoy, D., Merk, D., Painemal, D., Rausch, J., Rosenfeld, D., Russchenberg, H., Seifert, P., Sinclair, K., Stier, P., van Diedenhoven, B., Wendisch, M., Werner, F., Wood, R., Zhang, Z., and Quaas, J.: Remote sensing of droplet number concentration in warm clouds: a review of the current state of knowledge and perspectives, Rev. Geophys., 56, 409–453, https://doi.org/10.1029/2017RG000593, 2018.

Gryspeerdt, E. and Stier, P.: Regime-based analysis of aerosol-cloud interactions, Geophys. Res. Lett., 39, L21802, https://doi.org/10.1029/2012GL053221, 2012.

Gryspeerdt, E., Goren, T., Sourdeval, O., Quaas, J., Mülmenstädt, J., Dipu, S., Unglaub, C., Gettelman, A., and Christensen, M.: Constraining the aerosol influence on cloud liquid water path, Atmos. Chem. Phys., 19, 5331–5347, https://doi.org/10.5194/acp-19-5331-2019, 2019.

Hignett, P.: Observations of diurnal variation in a cloud-capped marine boundary layer, J. Atmos. Sci., 48, 1474–1482, 1991.

Hoffmann, F., Glassmeier, F., and Feingold, G.: The impact of aerosol on cloud water: a heuristic perspective, Atmos. Chem. Phys. 24, 13403–13412, https://doi.org/10.5194/acp-24-13403-2024, 2024.

Hoffmann, F., Chen, Y.-S., and Feingold, G.: On the processes determining the slope of cloud water adjustments in weakly and non-precipitating stratocumulus, Atmos. Chem. Phys., 25, 8657–8670, https://doi.org/10.5194/acp-25-8657-2025, 2025.

Kazil, J., Yamaguchi, T., and Feingold, G.: Mesoscale organization, entrainment, and the properties of a closed-cell stratocumulus cloud, J. Adv. Model. Earth Sy., 9, 2214–2229, https://doi.org/10.1002/2017MS001072, 2017.

Khairoutdinov, M. F. and Randall, D. A.: Cloud resolving modeling of the ARM summer 1997 IOP: model formulation, results, uncertainties, and sensitivities, J. Atmos. Sci., 60, 607–625, 2003.

Loeb, N. G., Kato, S., Loukachine, K., and Manalo-Smith, N.: Angular distribution models for top-of-atmosphere radiative flux estimation from the Clouds and the Earth's Radiant Energy System instrument on the Terra satellite. Part I: Methodology, J. Atmos. Ocean. Tech., 22, 338–351, 2005.

McCoy, I. L., Wood, R., and Fletcher, J. K.: Identifying meteorological controls on open and closed mesoscale cellular convection associated with marine cold air outbreaks, J. Geophys. Res.-Atmos., 122, 11678–11702, https://doi.org/10.1002/2017JD027031, 2017.

McCoy, I. L., McCoy, D. T., Wood, R., Zuidema, P., and Bender, F. A.-M.: The role of mesoscale cloud morphology in the shortwave cloud feedback, Geophys. Res. Lett., 50, e2022GL101042, https://doi.org/10.1029/2022GL101042, 2023.

Meskhidze, N., Remer, L. A., Platnick, S., Negrón Juárez, R., Lichtenberger, A. M., and Aiyyer, A. R.: Exploring the differences in cloud properties observed by the Terra and Aqua MODIS Sensors, Atmos. Chem. Phys., 9, 3461–3475, https://doi.org/10.5194/acp-9-3461-2009, 2009.

Muhlbauer, A., McCoy, I. L., and Wood, R.: Climatology of stratocumulus cloud morphologies: microphysical properties and radiative effects, Atmos. Chem. Phys., 14, 6695–6716, https://doi.org/10.5194/acp-14-6695-2014, 2014.

Mülmenstädt, J., Gryspeerdt, E., Dipu, S., Quaas, J., Ackerman, A. S., Fridlind, A. M., Tornow, F., Bauer, S. E., Gettelman, A., Ming, Y., Zheng, Y., Ma, P.-L., Wang, H., Zhang, K., Christensen, M. W., Varble, A. C., Leung, L. R., Liu, X., Neubauer, D., Partridge, D. G., Stier, P., and Takemura, T.: General circulation models simulate negative liquid water path–droplet number correlations, but anthropogenic aerosols still increase simulated liquid water path, Atmos. Chem. Phys., 24, 7331–7345, https://doi.org/10.5194/acp-24-7331-2024, 2024.

O, K.-T., Wood, R., and Bretherton, C. S.: Ultraclean layers and optically thin clouds in the stratocumulus-to-cumulus transition. Part II: Depletion of cloud droplets and cloud condensation nuclei through collision–coalescence, J. Atmos. Sci., 75, 1653–1673, 2018.

Pincus, R. and Baker, M. B.: Effect of precipitation on the albedo susceptibility of clouds in the marine boundary layer, Nature, 372, 250–252, 1994.

Platnick, S. and Twomey, S.: Determining the susceptibility of cloud albedo to changes in droplet concentration with the Advanced Very High Resolution Radiometer, J. Appl. Meteorol., 33, 334–347, 1994.

Platnick, S., Meyer, K. G., King, M. D., Wind, G., Amarasinghe, N., Marchant, B., Arnold, G. T., Zhang, Z., Hubanks, P. A., Holz, R. E., Yang, P., Ridgway, W. L., and Riedi, J.: The MODIS cloud optical and microphysical products: collection 6 updates and examples from Terra and Aqua, IEEE T. Geosci. Remote, 55, 502–525, 2016.

Possner, A., Wang, H., Wood, R., Caldeira, K., and Ackerman, T. P.: The efficacy of aerosol–cloud radiative perturbations from near-surface emissions in deep open-cell stratocumuli, Atmos. Chem. Phys., 18, 17475–17488, https://doi.org/10.5194/acp-18-17475-2018, 2018.

Possner, A., Eastman, R., Bender, F., and Glassmeier, F.: Deconvolution of boundary layer depth and aerosol constraints on cloud water path in subtropical stratocumulus decks, Atmos. Chem. Phys., 20, 3609–3621, https://doi.org/10.5194/acp-20-3609-2020, 2020.

Prabhakaran, P., Hoffmann, F., and Feingold, G.: Evaluation of pulse aerosol forcing on marine stratocumulus clouds in the context of marine cloud brightening, J. Atmos. Sci., 80, 1585–1604, 2023.

Rampal, N. and Davies, R.: On the factors that determine boundary layer albedo, J. Geophys. Res.-Atmos., 125, e2019JD032244, https://doi.org/10.1029/2019JD032244, 2020.

Rosenfeld, D., Kaufman, Y. J., and Koren, I.: Switching cloud cover and dynamical regimes from open to closed Benard cells in response to the suppression of precipitation by aerosols, Atmos. Chem. Phys., 6, 2503–2511, https://doi.org/10.5194/acp-6-2503-2006, 2006.

Rosenfeld, D., Wang, H., and Rasch, P. J.: The roles of cloud drop effective radius and LWP in determining rain properties in marine stratocumulus, Geophys. Res. Lett., 39, https://doi.org/10.1029/2012GL052028, 2012.

Rosenfeld, D., Zhu, Y., Wang, M., Zheng, Y., Goren, T., and Yu, S.: Aerosol-driven droplet concentrations dominate coverage and water of oceanic low-level clouds, Science, 363, eaav0566, https://doi.org/10.1126/science.aav0566, 2019.

Schneider, S. H. and Dickinson, R. E.: Parameterization of fractional cloud amounts in climatic models: the importance of modeling multiple reflections, J. Appl. Meteorol., 15, 1050–1056, 1976.

Stevens, B., Vali, G., Comstock, K., Wood, R., Van Zanten, M. C., Austin, P. H., Bretherton, C. S., and Lenschow, D. H.: Pockets of open cells and drizzle in marine stratocumulus, B. Am. Meteorol. Soc., 86, 51–57, https://doi.org/10.1175/BAMS-86-1-51, 2005.

Stevens, B., Bony, S., Brogniez, H., Hentgen, L., Hohenegger, C., Kiemle, C., L'Ecuyer, T. S., Naumann, A. K., Schulz, H., Siebesma, P. A., Vial, J., Winker, D. M., and Zuidema, P.: Sugar, gravel, fish and flowers: mesoscale cloud patterns in the trade winds, Q. J. Roy. Meteor. Soc., 146, 141–152, 2020.

Szczodrak, M., Austin, P. H., and Krummel, P. B.: Variability of optical depth and effective radius in marine stratocumulus clouds, J. Atmos. Sci., 58, 2912–2926, https://doi.org/10.1175/1520-0469(2001)058<2912:VOODAE>2.0.CO;2, 2001.

Toll, V., Christensen, M., Quaas, J., and Bellouin, N.: Weak average liquid-cloud-water response to anthropogenic aerosols, Nature, 572, 51–55, 2019.

Twomey, S.: Pollution and the planetary albedo, Atmos. Environ., 8, 1251–1256, 1974.

Twomey, S.: Aerosols, clouds and radiation, Atmos. Environ. A-Gen., 25, 2435–2442, 1991.

Wall, C. J., Norris, J. R., Possner, A., McCoy, D. T., McCoy, I. L., and Lutsko, N. J.: Assessing effective radiative forcing from aerosol–cloud interactions over the global ocean, P. Natl. Acad. Sci. USA, 119, e2210481119, https://doi.org/10.1073/pnas.2210481119, 2022.

Wang, H. and Feingold, G.: Modeling mesoscale cellular structures and drizzle in marine stratocumulus. Part I: Impact of drizzle on the formation and evolution of open cells, J. Atmos. Sci., 66, 3237–3256, https://doi.org/10.1175/2009JAS3022.1, 2009.

Watson-Parris, D., Sutherland, S., Christensen, M., Eastman, R., and Stier, P.: A large-scale analysis of pockets of open cells and their radiative impact, Geophys. Res. Lett., 48, e2020GL092213, https://doi.org/10.1029/2020GL092213, 2021.

Wolters, E. L. A., Deneke, H. M., van den Hurk, B. J. J. M., Meirink, J. F., and Roebeling, R. A.: Broken and inhomogeneous cloud impact on satellite cloud particle effective radius and cloud-phase retrievals, J. Geophys. Res., 115, D10214, https://doi.org/10.1029/2009JD012205, 2010.

Wood, R.: Relationships between optical depth, liquid water path, droplet concentration and effective radius in an adiabatic layer cloud, https://atmos.uw.edu/~robwood/papers/chilean_plume/optical_depth_relations.pdf (last access: 10 May 2026), 2006.

Wood, R.: Cancellation of aerosol indirect effects in marine stratocumulus through cloud thinning, J. Atmos. Sci., 64, 2657–2669, https://doi.org/10.1175/JAS3942.1, 2007.

Wood, R. and Hartmann, D. L.: Spatial variability of liquid water path in marine low cloud: the importance of mesoscale cellular convection, J. Climate, 19, 1748–1764, https://doi.org/10.1175/JCLI3702.1, 2006.

Wood, R., O, K.-T., Bretherton, C. S., Mohrmann, J., Albrecht, B. A., Zuidema, P., Ghate, V., Schwartz, C., Eloranta, E., and Glienke, S., Shaw, R. A., Fugal, J., and Minnis, P.: Ultraclean layers and optically thin clouds in the stratocumulus-to-cumulus transition. Part I: Observations, J. Atmos. Sci., 75, 1631–1652, 2018.

Wu, Y., Liu, J., Zhu, Y., Zhang, Y., Cao, Y., Huang, K.-E., Zheng, B., Wang, Y., Li, Y., Wang, Q., Zhou, C., Liang, Y., Sun, J., Wang, M., and Rosenfeld, D.: A global classification dataset of daytime and nighttime marine low-cloud mesoscale morphology based on deep-learning methods, Earth Syst. Sci. Data, 17, 3243–3258, https://doi.org/10.5194/essd-17-3243-2025, 2025.

Wyant, M. C., Bretherton, C. S., Rand, H. a., and Stevens, D. E.: Numerical simulations and a conceptual model of the stratocumulus to trade cumulus transition, J. Atmos. Sci., 54, 168–192, https://doi.org/10.1175/1520-0469(1997)054<0168:NSAACM>2.0.CO;2, 1997.

Yamaguchi, T., Feingold, G., and Kazil, J.: Stratocumulus to cumulus transition by drizzle, J. Adv. Model. Earth Sy., 9, 2333–2349, https://doi.org/10.1002/2017MS001104, 2017.

Yuan, T., Song, H., Wood, R., Mohrmann, J., Meyer, K., Oreopoulos, L., and Platnick, S.: Applying deep learning to NASA MODIS data to create a community record of marine low-cloud mesoscale morphology, Atmos. Meas. Tech., 13, 6989–6997, https://doi.org/10.5194/amt-13-6989-2020, 2020.

Zhang, J., Zhou, X., Goren, T., and Feingold, G.: Albedo susceptibility of northeastern Pacific stratocumulus: the role of covarying meteorological conditions, Atmos. Chem. Phys., 22, 861–880, https://doi.org/10.5194/acp-22-861-2022, 2022.

Zhou, X. and Feingold, G.: Impacts of mesoscale cloud organization on aerosol-induced cloud water adjustment and cloud brightness, Geophys. Res. Lett., 50, e2023GL103417, https://doi.org/10.1029/2023GL103417, 2023.

Zhou, X., Bretherton, C. S., Eastman, R., McCoy, I. L., and Wood, R.: Wavelet analysis of properties of marine boundary layer mesoscale cells observed from AMSR-E, J. Geophys. Res.-Atmos., 126, e2021JD034666, https://doi.org/10.1029/2021JD034666, 2021.